Comparing methods for measuring thickness, refractive index, and porosity of mesoporous thin films

Tiphaine Galy[a], Michal Marszewski[a], Sophia King[b], Yan Yan[b], Sarah H. Tolbert[b,c,d], Laurent Pilon[a,d,*]

[a] *Mechanical and Aerospace Engineering Department, Henry Samueli School of Engineering and Applied Science, University of California, Los Angeles*
[b] *Department of Chemistry and Biochemistry, University of California, Los Angeles*
[c] *Department of Materials Science and Engineering, Henry Samueli School of Engineering and Applied Science, University of California, Los Angeles*
[d] *The California NanoSystems Institute, University of California, Los Angeles*

A B S T R A C T

This study compares systematically contact profilometry, interferometry, ellipsometry, ellipsometric porosimetry, and nitrogen porosimetry for measuring thickness, effective refractive index, and/or porosity of mesoporous thin films. Indeed, such measurements are crucial in elucidating the structure-property relationships of mesoporous materials. Here, sol-gel and nanoparticle-based mesoporous silica and silica-titania thin films were synthesized and characterized using the aforementioned methods. The films were made by evaporation-induced self-assembly process using (i) tetraethyl orthosilicate and titanium isopropoxide as the silica and titania precursors or (ii) silica nanoparticles with a mean diameter of 9 nm as building blocks of the silica framework along with either Pluronic F127 or P123 block copolymers as structure directing agents. The synthesis recipe and deposition conditions were varied to achieve a wide range of compositions (silica:titania molar ratio from 100:0 to 70:30), thickness (80 nm $\leq L \leq$ 630 nm), effective refractive index (1.11 $\leq n_{eff,\lambda} \leq$ 1.75), porosity (0% $\leq \phi \leq$ 70%), and peak pore diameter (2.5 nm $\leq d_p \leq$ 20 nm). Overall, the thickness, effective refractive index, and/or porosity obtained from contact profilometry, interferometry, ellipsometry, and ellipsometric porosimetry agreed very well. However, porosity and pore size distribution obtained from nitrogen porosimetry on powder samples differed significantly from those of the equivalent thin films.

1. Introduction

Mesoporous thin films feature pores with diameter ranging from 2 to 50 nm [1] and thickness of up to a few microns [2]. They have been studied for their attractive optical [3–5], thermal [6,7], and mechanical properties [7–9] in many practical applications [3–5,8–12]. For example, mesoporous silica and TiO_2-P_2O_5 films have served as optical waveguides for evanescent-sensing techniques [4,10]. Indeed, covering the wave guiding layer with a mesoporous film enhanced the sensor's sensitivity if the film thickness was less than 2 to 3 times the penetration depth of the evanescent field [4,10]. In addition, mesoporous MgF_2, poly(methyl methacrylate) (PMMA), and poly(methyl silsesquioxane) (PMMSQ) films have been considered as antireflective coatings for solar cells [3,5]. To minimize reflectance of light at wavelength λ, the film must have (i) a thickness of $\lambda/4n_{eff,\lambda}$ and (ii) an effective refractive index $n_{eff,\lambda}$ equal to the geometric mean of the refractive indices of the surrounding medium $n_{1,\lambda}$ (= 1, if air) and of the

substrate $n_{3,\lambda}$, i.e., $n_{eff,\lambda} = (n_{1,\lambda} \; n_{3,\lambda})^{1/2}$ [13]. Finally, mesoporous silica, organosilicate, and polyimide films have been considered as interlayer dielectrics for microprocessor-based integrated circuits [8,9,11,12]. Here, the film dielectric constant (i.e., indirectly its refractive index) should be as small as possible to achieve a low signal propagation delay [8,9,11,12]. In all these applications, accurately and reliably measuring the thickness, effective refractive index, and porosity of mesoporous films is essential to ensure proper performance and quality control of the materials and devices.

The total porosity of mesoporous thin films can be divided into the connected (or open) porosity and the closed porosity corresponding to closed pores [14]. Porosity is an essential characteristic that affects the films' physical properties, including their refractive index [3,5], dielectric constant [8,9,11,12], thermal conductivity [6,7], and elastic modulus [7–9]. For example, Seino et al. [11] demonstrated that the effective refractive index decreased from 1.44 to 1.27 and the dielectric constant from 2.03 to 1.73 as the porosity of cubic mesoporous

Nomenclature

A, B, C	coefficients in Cauchy dispersion law
C_{N_2}	cross-sectional area of a nitrogen molecule, m^2
D	coefficient in Eq.(10), $D = (n_{eff,\lambda}^2 - 1)/(n_{eff,\lambda}^2 + 2)$
d_p	peak pore diameter, nm
L	mesoporous film thickness, nm
M	polymer to inorganic components mass ratio, g/g
M_w	molecular weight, Da
m_λ	complex index of refraction, $m_\lambda = n_\lambda - ik_\lambda$
N_A	Avogadro constant, $N_A = 6.02 \times 10^{23}$ mol^{-1}
N_m	monolayer capacity, mol/g
n_λ	refractive index
k_λ	absorption index
P	adsorbate pressure, Pa
P_0	adsorbate saturation pressure, Pa
$R_{pred,\lambda}$	predicted film reflectance, %
r_a	volume adsorbed ratio
r_λ	amplitude of the reflected wave
$r_{ij,\lambda}$	Fresnel's coefficient at the interface of media i and j
S_a	specific surface area, m^2/g
V_m	molecular volume of the adsorbate, cm^3
V_p	cumulative pore volume, cm^3/g
V_t	total pore volume, cm^3/g

Greek symbols

α_a	molecular polarizability of the adsorbate, cm^3
β_λ	phase difference, rad
Δ_λ	phase difference between $r_\perp$ and $r_\parallel$, rad
λ	wavelength of radiation, nm
μ	resistivity of the silicon substrate, Ω.cm
ϕ	total porosity, %
ϕ_o	open porosity, %
ρ	density of the solid phase, g/cm^3
$\tan \Psi_\lambda$	amplitude ratio of $r_\parallel/r_\perp$
Θ	angle of incidence or transmission, rad

Subscripts

1	refers to the surrounding medium, i.e., air
2	refers to the thin film
3	refers to the silicon substrate
c	refers to the continuous phase
d	refers to the dispersed phase
eff	refers to effective properties
$\perp$	refers to the perpendicular polarization
$\parallel$	refers to the parallel polarization

organosilica thin films increased from 4.4 to 39%. Coquil et al. [6] showed that the effective thermal conductivity of cubic and hexagonal mesoporous silica thin films depended mainly on their porosity and decreased non-linearly from 0.38 to 0.18 W/m.K as the porosity increased from 21 to 48%. Finally, Jain et al. [8] showed that the effective elastic modulus of xerogel mesoporous silica thin films decreased from 13 to 3.1 GPa as the porosity increased from 24 to 65%.

The thickness of thin films can be measured by contact profilometry using a stylus to measure the distance between the substrate and the film top surface. Note that this method is destructive and requires to form a deep scratch through the film down to the substrate. Alternatively, the thickness of thin films can be measured using optical techniques such as (a) interferometry measuring the spectral reflectance for unpolarized light [15] and (b) ellipsometry measuring the spectral reflectance for polarized light [3,4,7,8]. Note that these methods are applicable only to transparent or semi-transparent (i.e., optically thin) films. Interferometry and ellipsometry measurements yield the effective refractive index in addition to the film thickness. Then, the porosity of the films can be retrieved by using an effective medium approximation (EMA) [3]. Moreover, porosity and pore size distribution can be measured using ellipsometric porosimetry consisting of measuring the reflectance of polarized light while a gas or vapor is progressively adsorbed into the mesoporous films [11,16]. Finally, for bulk mesoporous samples, porosity and pore size distribution can be measured using gas adsorption methods such as nitrogen porosimetry [1]. However, characterization of mesoporous thin films by nitrogen porosimetry is challenging due to their small mass [16]. To address this limitation, nitrogen porosimetry on powders prepared using the same method as that used for the thin films has been used [17–19].

The present study compares systematically the results of the different methods commonly used for measuring thickness, effective refractive index, porosity, and/or pore size distribution of mesoporous thin films. To do so, various sol-gel mesoporous silica-titania films as well as nanoparticle-based mesoporous silica films were synthesized with different thicknesses, structures, compositions, porosities, and pore size distributions. Then, the synthesized films and their equivalent powders were systematically characterized by contact profilometry, interferometry, ellipsometry, ellipsometric porosimetry, and nitrogen porosimetry.

2. Background

2.1. Effective medium approximations

Effective medium approximations (EMAs) treat heterogeneous materials as homogeneous with some effective properties. For example, EMAs predict the effective refractive index of heterogeneous media based on the optical properties and volume fractions of its constituent materials, assumed to be known. For mesoporous materials, this approach is valid if the pore size is much smaller than the wavelength λ of the incident light so that scattering by pores can be ignored [2,20,21]. In addition, the films should be thick compared to the pore size to consider a sufficiently large representative volume of the film [22,23].

The most commonly used EMAs include (1) the symmetric Bruggeman model [20,21,24], (2) the Maxwell-Garnett model [25], (3) the asymmetrical Bruggeman model [26], (4) the Lorentz-Lorenz model [27,28], and (5) the volume averaging theory (VAT) [22]. The symmetric Bruggeman model relates the effective refractive index of a two-phase mixture $n_{eff,\lambda}$ to its total porosity ϕ as [20]

$$\phi \frac{n_{d,\lambda}^2 - n_{eff,\lambda}^2}{n_{d,\lambda}^2 + 2n_{eff,\lambda}^2} + (1 - \phi) \frac{n_{c,\lambda}^2 - n_{eff,\lambda}^2}{n_{c,\lambda}^2 + 2n_{eff,\lambda}^2} = 0 \tag{1}$$

where the subscript "c" refers to the "continuous" phase (e.g., silica), and the subscript "d" refers to the "dispersed" phase (e.g., air or toluene). Similarly, the Maxwell-Garnett model was derived for randomly monodisperse spherical inclusions in a continuous matrix and is expressed as [20]

$$n_{eff,\lambda}^2 = n_{c,\lambda}^2 \left[1 - \frac{3\phi(n_{c,\lambda}^2 - n_{d,\lambda}^2)}{2n_{c,\lambda}^2 + n_{d,\lambda}^2 + \phi(n_{c,\lambda}^2 - n_{d,\lambda}^2)} \right]. \tag{2}$$

The asymmetrical Bruggeman model considers polydisperse spheres distributed in a continuous matrix [29]. It predicts the effective refractive index $n_{eff,\lambda}$ of the mesoporous material based on the following implicit relationship [20]

$$1 - \phi = \frac{\frac{n_{eff,\lambda}^2}{n_{c,\lambda}^2} - \frac{n_{d,\lambda}^2}{n_{c,\lambda}^2}}{\left(\frac{n_{eff,\lambda}^2}{n_{c,\lambda}^2}\right)^{1/3}\left(1 - \frac{n_{d,\lambda}^2}{n_{c,\lambda}^2}\right)}. \tag{3}$$

The Lorentz-Lorenz model was derived for monodisperse spherical particles in air and expresses the effective refractive index implicitly according to [30–32]

$$\frac{n_{eff,\lambda}^2 - 1}{n_{eff,\lambda}^2 + 2} = (1 - \phi)\frac{n_{c,\lambda}^2 - 1}{n_{c,\lambda}^2 + 2} + \phi\frac{n_{d,\lambda}^2 - 1}{n_{d,\lambda}^2 + 2}. \tag{4}$$

The Maxwell-Garnett and Bruggeman models have been generalized to ellipsoidal and spheroidal inclusions to account for the shape and orientation of the inclusions [33–35]. On the other hand, the VAT model was derived by volume averaging the Maxwell's equations and disregards the inclusions shape, size, and spatial distribution. It expresses the effective refractive index $n_{eff,\lambda}$ of a non-absorbing two-phase composite as [36]

$$n_{eff,\lambda}^2 = \phi n_{d,\lambda}^2 + (1 - \phi)n_{c,\lambda}^2. \tag{5}$$

Hutchinson et al. [23,37] numerically solved Maxwell's equations through mesoporous silica films with different porosities and morphologies and compared the porosity retrieved from different EMAs based on reflectance spectrum simulated numerically. The authors concluded that the Maxwell-Garnett model could predict the effective refractive index $n_{eff,\lambda}$ while the asymmetrical Bruggeman model predicted the absorption index $k_{eff,\lambda}$ of mesoporous films with spherical pores regardless of their spatial arrangement. Similarly, Braun and Pilon [22] recommended the VAT model for non-absorbing films consisting of aligned cylindrical pores in a continuous matrix. Stenzel [2] recommended the Lorentz-Lorenz model for highly porous films regardless of their morphology. Despite the different recommendations, the above mentioned EMAs yield similar predictions for mesoporous materials with relatively small mismatch in refractive indices between the continuous and the dispersed phases such as mesoporous silica (see Fig. S1 in Supporting Information).

2.2. Interferometry

Interferometry relies on interference patterns present in UV–Vis reflectance spectra of thin films to measure their thickness and refractive index. The theoretical spectral reflectance of a non-absorbing, non-scattering, optically homogeneous, and isotropic thin film deposited on a reflective substrate (Fig. 1) for unpolarized light can be expressed as [13]

$$R_{pred,\lambda} = \frac{|r_{\perp,\lambda}|^2 + |r_{\parallel,\lambda}|^2}{2} \tag{6}$$

where $r_{\perp,\lambda}$ and $r_{\parallel,\lambda}$ are the amplitude reflection coefficients for the perpendicular and parallel polarizations, respectively. They can be expressed as [13]

$$r_{\perp,\lambda} = \frac{r_{12,\perp,\lambda} + r_{23,\perp,\lambda}e^{-2i\beta_\lambda}}{1 + r_{12,\perp,\lambda}r_{23,\perp,\lambda}e^{-2i\beta_\lambda}} \quad \text{and} \quad r_{\parallel,\lambda} = \frac{r_{12,\parallel,\lambda} + r_{23,\parallel,\lambda}e^{-2i\beta_\lambda}}{1 + r_{12,\parallel,\lambda}r_{23,\parallel,\lambda}e^{-2i\beta_\lambda}} \tag{7}$$

where $r_{12,\lambda}$ and $r_{13,\lambda}$ are the Fresnel's coefficients defined as [13]

$$r_{ij,\perp,\lambda} = \frac{m_{i,\lambda}\cos\theta_i - m_{j,\lambda}\cos\theta_j}{m_{i,\lambda}\cos\theta_i + m_{j,\lambda}\cos\theta_j} \quad \text{and} \quad r_{ij,\parallel,\lambda} = \frac{m_{j,\lambda}\cos\theta_i - m_{i,\lambda}\cos\theta_j}{m_{j,\lambda}\cos\theta_i + m_{i,\lambda}\cos\theta_j}. \tag{8}$$

Here, $m_{1,\lambda} = n_{1,\lambda}$ is the refractive index of the transparent surrounding medium, $m_{2,\lambda} = n_{2,\lambda}$ is the refractive index of the non-absorbing film, and $m_{3,\lambda} = n_{3,\lambda} - ik_{3,\lambda}$ is the complex refractive index of the substrate. In addition, $\beta_\lambda = 2\pi n_{2,\lambda}L\cos\theta_2/\lambda$ is the phase difference between interfering waves while θ_1 is the angle of the collimated incident radiation defined with respect to the outward normal vector to

the film. Moreover, θ_2 is the angle of transmission at the air/film interface and θ_3 is a complex angle [13]. The angles θ_2 and θ_3 can be calculated using Snell's law [13] according to $n_{1,\lambda}\sin\theta_1 = n_{2,\lambda}\sin\theta_2$ and $n_{2,\lambda}\sin\theta_2 = m_{3,\lambda}\sin\theta_3$. If the substrate is non-absorbing, θ_3 is real and corresponds to the angle of transmission at the film/substrate interface (Fig. 1).

Fitting the experimental reflectance spectrum from a thin film on a substrate of known optical properties $m_{3,\lambda}$ using Equations (6)–(8) yields the thickness L and refractive index $n_{2,\lambda}$ of the film. When the film is absorbing, the complex refractive index $m_{2,\lambda}$ can also be retrieved by interferometry by including the adsorption index $k_{2,\lambda}$ in the fitting procedure. Note that this procedure also requires prior knowledge of the complex index of refraction of the surrounding medium $m_{1,\lambda}$ (if different from air) and of the incident angle θ_1. Furthermore, Equation (7) is valid when the substrate is thick enough to be treated as semi-infinite. Finally, a reflective substrate is preferred to maximize the signal-to-noise ratio and to measure strong interference fringes.

For mesoporous thin films, this procedure retrieves the effective refractive index $n_{eff,\lambda}$ ($= n_{2,\lambda}$) that can then be used to retrieve the porosity ϕ based on some EMAs. In this study, the Maxwell-Garnett model [Equation (2)] was chosen for $n_{eff,\lambda}$ since it was validated both numerically [23] and experimentally [37] for sol-gel mesoporous silica films. Moreover, note that the porosity ϕ retrieved by interferometry based on some EMAs is the total porosity including both the open and closed porosities. By contrast, porosimetry techniques, including ellipsometric porosimetry and nitrogen porosimetry, measure only the open porosity ϕ_o accessible to the probing molecule. Fig. S2(a) in Supporting Information illustrates the procedure of interferometry used in the present study.

2.3. Ellipsometry

Spectroscopic ellipsometry measures changes in polarization between the linearly polarized incident radiation and the reflected radiation from a film as a function of wavelength in the UV to IR regions. After reflection by the film and its substrate, the polarization of the electromagnetic wave changes from linear to elliptical. The measured reflected intensity is characterized by two angles Δ_λ and Ψ_λ where Δ_λ represents the phase difference between the parallel and perpendicular polarizations of the reflected electric field while $\tan\Psi_\lambda$ represents the change in their amplitude ratio. The amplitude reflection coefficients $r_{\perp,\lambda}$ and $r_{\parallel,\lambda}$ of the perpendicular and parallel components of polarization are such that their ratio is given by [38]

$$\frac{r_{\parallel,\lambda}}{r_{\perp,\lambda}} = \tan\Psi_\lambda\exp(i\Delta_\lambda). \tag{9}$$

For a mesoporous thin film on a reflective substrate, the ratio $r_{\parallel,\lambda}/r_{\perp,\lambda}$ depends on the film's thickness L and on its effective refractive index $n_{eff,\lambda}$ [Equation (7)]. Therefore, fitting the spectral angles Δ_λ and
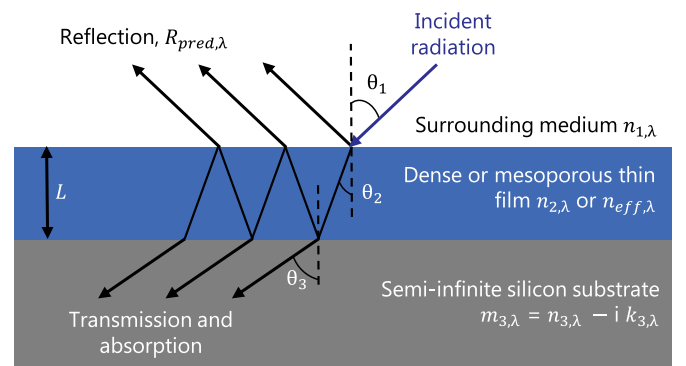

Fig. 1. Schematic of dense or mesoporous thin films deposited on a silicon substrate exposed to collimated light incident at angle θ_1.

Ψ_λ to a model based on thin film optics enables the retrieval of both L and $n_{eff,\lambda}$ of non-absorbing mesoporous thin films. Then, $n_{eff,\lambda}$ can be used to calculate the total porosity ϕ of the film using one of the EMAs previously discussed.

2.4. Ellipsometric porosimetry

Ellipsometric porosimetry (EP) combines ellipsometry and gas adsorption measurements by measuring the mesoporous thin film's thickness and refractive index as a gas (i.e., adsorbate) progressively fills the pores. This method yields (i) the thickness L, (ii) the spectral effective refractive index $n_{eff,\lambda}$, (iii) the adsorption and desorption isotherms, (iv) the open porosity ϕ_o, and (v) the pore size distribution. The thickness L and the effective refractive index $n_{eff,\lambda}$ are retrieved by the ellipsometry method previously described. This method is also used to retrieve the thicknesses $L(P)$ and effective refractive indices $n_{eff,\lambda}(P)$ of the film filled with adsorbate retrieved for different pressures P. Then, the amount of adsorbate adsorbed/desorbed in the mesoporous film can be calculated as a function of the relative pressure P/P_0 where P_0 is the adsorbate saturation pressure. Since the processes are not necessarily reversible, the resulting adsorption and desorption isotherms feature hysteresis loops that can be classified into four types and provide information on the pore connectivity and shape [1]. In the case of ellipsometric porosimetry, the volume adsorbed ratio $r_a(P)$ at adsorbate pressure P, defined as the ratio of the volume of adsorbate in pores to the volume occupied by the film, is calculated from the thickness $L(P)$ and effective refractive index $n_{eff,\lambda}(P)$ using some EMA. For example, when using the Lorentz-Lorenz model, the volume adsorbed ratio $r_a(P)$ can be expressed as [27]

$$r_a(P) = \frac{V_m}{\alpha_a L(P)}[D(P)L(P) - D(0)L(0)] \tag{10}$$

where V_m is the molecular volume of the adsorbate (in cm^3), α_a is the molecular polarizability of the adsorbate (in cm^3), and $D(P)$ is defined as $D(P) = [n_{eff,\lambda}(P)^2 - 1]/[n_{eff,\lambda}(P)^2 + 2]$.

Then, the open porosity ϕ_o is calculated using the Lorentz-Lorenz EMA [Equation (4)] based on the effective refractive indices measured when the pores are completely empty and when the accessible pores are completely filled with the adsorbate close to saturation P_0 such that

$$\phi_o = r_a(P_0) = \frac{D(P_0) - D(0)}{\frac{n_{d,\lambda}(P_0)^2 - 1}{n_{d,\lambda}(P_0)^2 + 2}} \tag{11}$$

where $n_{d,\lambda}(P_0)$ is the refractive index of the adsorbate, assumed to be known.

Finally, the pore size distribution can be calculated from the isotherms using the Barrett-Joyner-Halenda (BJH) [39] algorithm which assumes that the pores are cylindrical. The model relies on the Kelvin equation relating the pore filling pressure to the radius of curvature of the adsorbate phase [40]. This estimate is then corrected for the layer of adsorbate present on the pore walls, using the measured or estimated statistical film thickness curve [41]. Fig. S2(b) in Supporting Information shows a diagram of the procedure.

2.5. Nitrogen porosimetry

Nitrogen porosimetry is a gas adsorption technique that measures (i) adsorption and desorption isotherms, (ii) the specific surface area S_a (in m^2/g), (iii) the total pore volume V_t (in cm^3/g) and open porosity ϕ_o, and (iv) the pore size distribution of bulk mesoporous materials. Adsorption-desorption isotherms report the amount of adsorbed nitrogen, calculated from the difference in numbers of moles that are (i) dosed into the sample tube and (ii) left in the gas phase in the sample tube after adsorption is complete, as a function of the relative pressure P/P_0. The specific surface area S_a can be obtained by the Brunauer-Emmett-Teller (BET) method based on the expression [42]

$$S_a = N_A C_{N_2} N_m \tag{12}$$

where N_A is the Avogadro constant (in mol^{-1}) and C_{N_2} is the cross-sectional area of a N_2 molecule adsorbed in a monolayer (in m^2) while N_m is the measured monolayer capacity (in mol/g), defined as the number of moles of N_2 needed to cover the surface of the pores in 1 g of porous material with a monolayer of N_2. The total pore volume V_t can be calculated by converting the number of moles of nitrogen adsorbed at a relative pressure P/P_0 close to saturation to the volume of liquid nitrogen based on the liquid nitrogen molar density of 34.38 cm^{3}mol^{-1} [14,43]. Then, the open porosity ϕ_o can be calculated from the total pore volume V_t according to [14]

$$\phi_o = \frac{V_t \rho}{1 + V_t \rho} \tag{13}$$

where ρ is the density of the solid phase. Here also, the pore size distribution of mesoporous materials is obtained from the BJH method [39] using the Kelvin equation and the statistical film thickness of the adsorbate on the pore walls to estimate the pore size [44]. Nitrogen porosimetry is mainly used for characterizing mesoporous powders available in sufficiently large quantities.

Interferometry is a simple and well-established technique for measuring thickness and refractive index of dense thin films and has been implemented in commercial devices [45]. Several studies used interferometry to retrieve thickness and effective refractive index of mesoporous thin films and to estimate their porosity using some EMAs [15,46–48]. However, to the best of our knowledge, no comprehensive comparison of interferometry with other well-established methods for measuring the thickness, effective refractive index, and porosity of mesoporous thin films is available in the literature. Notably, this method has never been used for multicomponent mesoporous thin films such as silica-titania films. In addition, this study aims at determining if nitrogen porosimetry measurements on equivalent powders can be used as a substitute to measurements on thin films.

3. Materials and methods

3.1. Materials

The following materials were obtained from commercial suppliers and used without further purification: (1) ammonia-stabilized colloidal suspension of silica nanoparticles (15 wt% of silica in water, measured mean particle diameter 9 nm, Nalco 2326, Nalco Chemical Company), (2) triblock copolymer Pluronic P123 (EO$_{20}$PO$_{70}$EO$_{20}$, M_w = 5800 Da, BASF), (3) triblock copolymer Pluronic F127 (EO$_{100}$PO$_{65}$EO$_{100}$, M_w = 12600 Da, BASF), (4) tetraethyl orthosilicate (TEOS) (98%, Acros Organics), (5) titanium isopropoxide (TIPO) (95%, Acros Organics), (6) hydrochloric acid (38 wt% in water, Certified ACS Plus, Fisher Scientific), (7) and ethanol (200 proof, Rossville Gold Shield).

3.2. Synthesis

Mesoporous silica and silica-titania thin films were prepared by evaporation-induced self-assembly [49–51] using either molecular precursors of silica (TEOS) and titania (TIPO) or silica nanoparticles as the building blocks along with Pluronic F127 or P123 as the structure directing agents. The porosity, pore size, and pore wall thickness of the thin films were controlled by adjusting the mass ratio M of the polymer to the inorganic components (i.e., the sum of silica and titania). The exact synthesis is described in the following paragraphs. Note that nanoparticle-based mesoporous silica-titania films were not prepared because solutions of silica and titania nanoparticles were unstable due to uncontrolled aggregation and precipitation caused by their opposing surface charges. Indeed, the silica nanoparticles were stabilized in NH$_3$ at pH 9 resulting in a negative surface charge while the titania nanoparticles were stabilized in solution at pH 3 resulting in a positive

surface charge [52].

3.2.1. Mesoporous silica thin films

The solution of molecular silica precursor was prepared by dissolving 25 mg of either Pluronic F127 or Pluronic P123 in 0.6 mL of ethanol and 0.16 mL of 0.05 M aqueous HCl by magnetic stirring. Then, TEOS was added in the amount corresponding to the desired polymer to silica mass ratio M between 0.1 and 2.5 g/g. Similarly, the solution of silica nanoparticles and structure directing agents was prepared by dissolving 0.678 g of either Pluronic F127 or Pluronic P123 in 3 mL of deionized water by magnetic stirring. Then, the colloidal suspension of silica nanoparticles was added in the amount corresponding to M between 0.1 and 2 g/g.

Sol-gel and nanoparticle-based mesoporous silica thin films were synthesized by spin-coating 80 μL of one of the above solutions onto a 1″ x 1″ single-crystal p-doped silicon substrate (μ = 0.005–0.01 Ω.cm). The film thickness was varied by changing the spin speed between 1000 and 4000 rpm. The as-spun films were calcined in air at 350°C for 30 min using a temperature ramp of 2°C/min to remove the polymer and then cooled in air to room temperature.

3.2.2. Silica-titania thin films

The synthesis of sol-gel mesoporous silica-titania films was adapted from the literature [53]. The desired amount of Pluronic F127 was dissolved in a solution of ethanol, HCl, and H_2O that was rapidly stirred at 60°C. Then, the desired amount of TEOS was added to the solution followed by a dropwise addition of TIPO, and the stirring was continued for another 5 h at 60°C. The amount of Pluronic F127 was adjusted to correspond to a polymer to inorganic components mass ratio M between 1 and 2.5 g/g while the amount of the remaining components of the solution were defined by a molar ratio ethanol:HCl:H_2O:TIPO:TEOS = 50:6.1:0.06:x:(1-x) where x = 0.1, 0.2, and

0.3 determined the molar ratio of silica and titania in the prepared thin films. The sol-gel mesoporous silica-titania thin films were synthesized by spin-coating (1000–4000 rpm) 80 μL of the above silica-titania solution onto a 1″ x 1″ single-crystal p-doped silicon substrate (μ = 0.005–0.01 Ω.cm). The as-spun films were calcined in flowing oxygen at 400°C for 2 h using a temperature ramp of 1°C/min to remove the polymer and then cooled in flowing oxygen to room temperature.

Moreover, dense (i.e., non-porous) sol-gel silica-titania thin films with compositions identical to those of the sol-gel mesoporous silica-titania films were prepared using the same procedure but without Pluronic F127. These films were used to measure the refractive index of the silica-titania continuous phase $n_{c,\lambda}$ necessary to retrieve porosity of the sol-gel mesoporous silica-titania films using an EMA.

3.2.3. Mesoporous silica and silica-titania powders

Finally, sol-gel and nanoparticle-based mesoporous silica powders and sol-gel mesoporous silica-titania powders were synthesized from the same solutions as those used to prepare the corresponding silica and silica-titania thin films. The solutions were evaporated in a Petri dish for at least 2 days, at relative humidity above 50%. The resulting powders were calcined in a tube furnace in flowing oxygen at 400°C for 10–12 h using a temperature ramp of 5°C/min to remove the polymer template. They were then cooled in flowing oxygen to room temperature. These powders were characterized by nitrogen porosimetry.

3.3. Characterization

Mesoporous thin films were characterized by (i) scanning electron microscopy (SEM), (ii) contact profilometry, (iii) interferometry, (iv) ellipsometry, and (v) ellipsometric porosimetry (EP). Note that the porosity retrieved by interferometry and ellipsometry combined with the Maxwell-Garnett model corresponded to the total porosity ϕ of the

Table 1

Structure, composition, thickness L, spectral effective refractive index $n_{eff,\lambda}$, and open porosity ϕ_o of the different mesoporous sol-gel silica (SG) and silica-titania (ST) thin films and nanoparticle-based silica (NP) films investigated in the present study.

Sample	Structure	Polymer	Mass ratio M (g/g)	Silica:titania molar ratio	Film thickness L (nm)	Effective refractive index $n_{eff,\lambda}$ (λ = 400–800 nm)	Open porosity ϕ_o (%)	Peak pore diameter d_p (nm)
SGF-2.5	sol-gel	F127	2.5	100:0	628	1.11	58	15.2
SGF-2	sol-gel	F127	2	100:0	374	1.17-1.18	65	11.5
SGF-1.7	sol-gel	F127	1.7	100:0	235	1.22	45	8.1
SGF-1.4	sol-gel	F127	1.4	100:0	255	1.22	46	8.1
SGF-1.2	sol-gel	F127	1.2	100:0	198	1.25-1.26	41	8.7
SGF-1.2-2	sol-gel	F127	1.2	100:0	337	1.20-1.21	54	15
SGF-0.6	sol-gel	F127	0.6	100:0	156	1.35	31	7.6
SGF-0.4	sol-gel	F127	0.4	100:0	231	1.37-1.39	22	6
SGP-1.5	sol-gel	P123	1.5	100:0	460	1.18-1.19	65	5.2
SGP-0.8	sol-gel	P123	0.8	100:0	297	1.23-1.24	47	8
SGP-0.2	sol-gel	P123	0.2	100:0	80.5	1.41	8	2.5
NPF-1.7	NP	F127	1.7	100:0	526	1.15-1.6	59	16.4
NPF-1.5	NP	F127	1.5	100:0	524	1.15-1.16	40	13.9
NPF-1.2	NP	F127	1.2	100:0	401	1.21-1.22	53	13.3
NPF-1.2-2	NP	F127	1.2	100:0	530	1.21-1.22	61	12.7
NPF-1	NP	F127	1	100:0	368	1.19-1.20	55	10.8
NPF-0.5	NP	F127	0.5	100:0	406	1.29	33	5.8
NPF-0.3	NP	F127	0.3	100:0	399	1.29-1.30	34	2.8
NPP-2	NP	P123	2	100:0	456	1.19	56	12.3
NPP-1.5	NP	P123	1.5	100:0	461	1.17-1.18	68	13.2
NPP-0.5	NP	P123	0.5	100:0	396	1.25-1.26	40	6.4
NPP-0.2	NP	P123	0.2	100:0	438	1.27-1.28	36	4.4
STF91-1	sol-gel	F127	1	90:10	242	1.33-1.35	36	4.1
STF82–2.2	sol-gel	F127	2.2	80:20	571	1.27	58	4.5
STF82-2	sol-gel	F127	2	80:20	508	1.28	53	4.9
STF82–1.7	sol-gel	F127	1.7	80:20	445	1.29-1.31	42	4
STF82–1.5	sol-gel	F127	1.5	80:20	424	1.32-1.34	41	4
STF82-1	sol-gel	F127	1	80:20	321	1.32-1.37	39	3.7
STF73–1.5	sol-gel	F127	1.5	70:30	452	1.33-1.35	48	4
STF73-1	sol-gel	F127	1	70:30	369	1.40-1.43	32	4

mesoporous films while that measured by ellipsometric porosimetry represented the open porosity ϕ_o [14]. The open porosity of mesoporous powders was characterized by low-temperature nitrogen porosimetry. All details of these measurements and calculations are provided in Supporting Information.

4. Results and discussion

Table 1 summarizes the structure, composition, thickness L, spectral effective refractive index $n_{eff,\lambda}$, open porosity ϕ_o, and peak pore diameter d_p, characterized by ellipsometric porosimetry, for sol-gel silica (denoted by SG) and silica-titania (ST) as well as nanoparticle-based silica (NP) mesoporous thin films using Pluronic F127 (F) or P123 (P) with different polymer to inorganic components mass ratio M. Here, the pore size distribution was calculated from the adsorption branch of the isotherm and the peak pore diameter d_p was defined as the diameter for which the pore size distribution reached its maximum. In the following discussion, ellipsometric porosimetry was used as the reference method to characterize mesoporous thin films.

4.1. Scanning electron microscopy

Fig. 2 shows SEM images of three representative mesoporous thin films namely (a) SGF-1.2 sol-gel silica film prepared using Pluronic F127 with polymer to silica mass ratio $M = 1.2\,\mathrm{g/g}$, (b) NPP-1.5 nanoparticle-based silica film prepared using Pluronic P123 with $M = 1.5\,\mathrm{g/g}$, and (c) STF73–1.5 sol-gel silica-titania film prepared using Pluronic F127 with $M = 1.5\,\mathrm{g/g}$ and a silica:titania molar ratio of 70:30. The images indicate that the films were mesoporous with somewhat uniform but disordered pores. The backbone of the sol-gel silica and silica-titania films consisted of continuous silica and silica-titania networks that were created by condensation of the molecular precursor(s) [Fig. 2(a)–(c)]. By contrast, the backbone of the nanoparticle-based silica film consisted of a network of aggregated silica nanoparticles that served as building blocks of the mesoporous structure [Fig. 2(b)].

4.2. Reference measurements

4.2.1. Refractive index of dense silica-titania $n_{c,\lambda}$

Fig. 3 plots the spectral refractive index $n_{c,\lambda}$ of dense silica-titania films for wavelength λ between 400 and 800 nm retrieved by interferometry and ellipsometry for silica:titania molar ratio of 100:0 [54], 90:10, 80:20, and 70:30 using Cauchy's dispersion law given by [41]

$$n_{c,\lambda} = A + \frac{B}{\lambda^2} + \frac{C}{\lambda^4} \tag{14}$$

where A, B (in μm^2), and C (in μm^4) are fitting coefficients with λ expressed in μm. First, Fig. 3 shows that the refractive index $n_{c,\lambda}$ measured by interferometry was in very good agreement with that measured by ellipsometry. Table S1 summarizes the values of A, B, and C for the different silica:titania molar ratios considered. In fact, the relative error in the refractive index $n_{c,\lambda}$ between the two methods was less than 6% (Table S2 and Fig. S3).

Fig. 3 also indicates that the refractive index of the dense silica-titania films increased with decreasing silica:titania molar ratio. This was expected since amorphous titania has a larger refractive index than silica [55], i.e., 2–2.6 vs. 1.45 in the 400–800 nm wavelength range. In addition, the refractive index $n_{c,\lambda}$ of dense silica-titania films varied from 0.03 to 0.07 in the 400–800 nm wavelength range as the silica:-titania molar ratio ranged from 90:10 to 70:30 while that of silica did not vary by more than 0.02. Thus, the spectral nature of the refractive index of silica-titania $n_{c,\lambda}$, given by the dispersion law of Equation (14), must be considered in order to achieve good fitting of the reflectance spectra. However, the refractive index $n_{c,\lambda}$ of silica can be assumed to be constant and equal to 1.459 (see section S1 in Supporting Information).

4.2.2. Adsorption-desorption isotherms

Fig. 4 shows toluene adsorption-desorption isotherms of the (a) sol-gel mesoporous silica films (SGF), (b) nanoparticle-based mesoporous silica films (NPF), and (c) sol-gel mesoporous silica-titania films (STF) with silica:titania molar ratios of 90:10, 80:20, and 70:30 all prepared using Pluronic F127 with different polymer to inorganic components mass ratio M. All isotherms were of the type IV(a) according to the
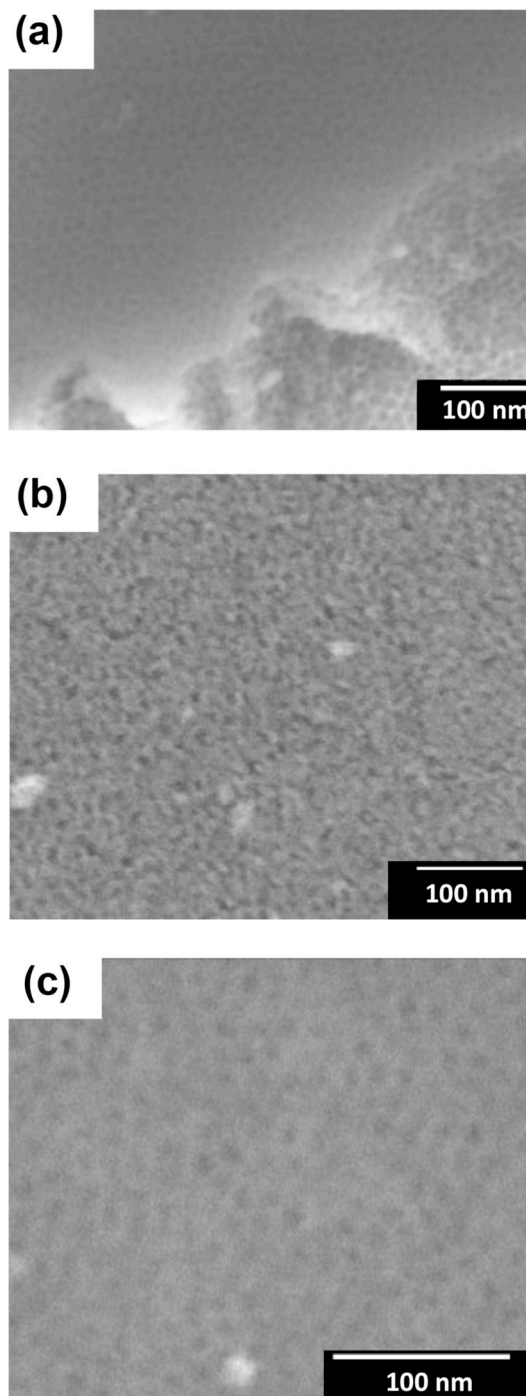

Fig. 2. SEM images of (a) sol-gel mesoporous silica film templated with Pluronic F127 with a mass ratio M of 1.2 g/g (SGF-1.2), (b) nanoparticle-based mesoporous silica film templated with Pluronic P123 with $M = 1.5\,\mathrm{g/g}$ (NPP-1.5), and (c) sol-gel mesoporous silica-titania film templated with Pluronic F127 and $M = 1.5\,\mathrm{g/g}$ and with a silica:titania molar ratio of 70:30 (STF73–1.5). Silica matrix or nanoparticles appear in grey and pores appear in black.
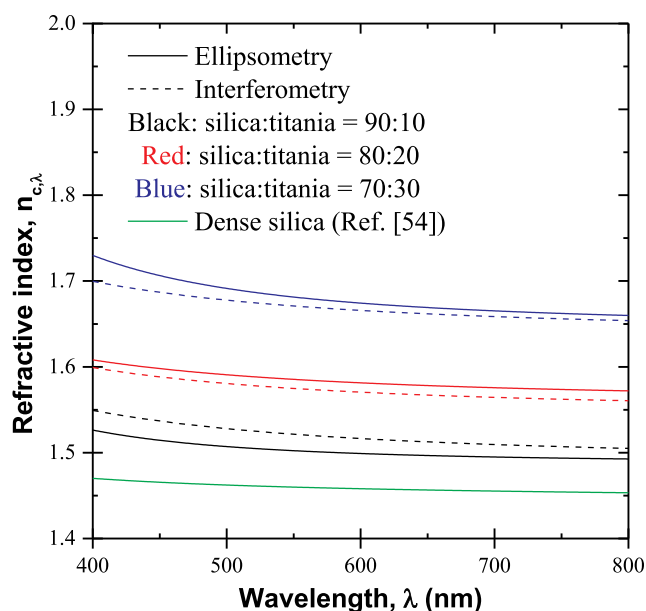
Fig. 3. Spectral refractive index $n_{c,\lambda}$ of dense silica-titania films with silica:titania molar ratio of 90:10, 80:20, and 70:30 retrieved from ellipsometry (solid lines) and interferometry (dashed lines). The refractive index of silica from Ref. [54] is also plotted for comparison.

IUPAC classification [1] confirming that all films were mesoporous. The isotherms of the sol-gel mesoporous (i) silica films with a mass ratio M < 2 g/g and (ii) silica-titania films featured H2(a) hysteresis loops indicating that the mesopores were constricted by necks with narrow size distribution [1]. The latter resulted in pore-blocking apparent through the very steep desorption close to the cavitation point of toluene. This indicates that the pores were likely spherical and the narrow connections between them served as the constricting necks. The isotherms of (a) the sol-gel mesoporous silica films prepared using Pluronic F127 with M = 2 and 2.5 g/g (SGF-2 and SGF-2.5) and (b) all nanoparticle-

based mesoporous silica films prepared using Pluronic F127 featured H2(b) hysteresis loops indicating that the mesopores were similarly constricted by necks but in these films the neck size distribution was broader [1]. The latter was likely due to the broader pore size distributions in the sol-gel films with high mass ratio M and in all nanoparticle-based films.

Fig. S4 in Supporting Information presents the toluene adsorption-desorption isotherms of the sol-gel mesoporous silica films (SGP-0.2 to 1.5) and of the nanoparticle-based mesoporous silica films (NPP-0.2 to 2) templated with Pluronic P123, instead of Pluronic F127. Fig. S4(a) shows that SGP-0.2 had an isotherm of type I(b) and featured an irreversible adsorption isotherm, i.e., the adsorption and desorption branches did not coincide even below the cavitation point of toluene, likely due to trapping of toluene in the network of very small pores. This was likely due to the very small amounts of block copolymer used for the synthesis of this film that resulted in small pores [1]. The isotherms of the other sol-gel and nanoparticle-based silica films prepared using Pluronic P123 were all of the type IV(a) indicating the presence of mesopores [1]. The SGP-0.8 film featured an H2(a) hysteresis loop while the SGP-1.5, NPP-0.2, NPP-0.5, NPP-1.5, and NPP-2 films featured H2(b) hysteresis loops.

4.2.3. Porosity

Fig. 5 depicts the open and total porosities retrieved by ellipsometric porosimetry and by interferometry for (a) sol-gel mesoporous silica, (b) nanoparticle-based mesoporous silica, and (c) sol-gel mesoporous silica-titania films (see Table 1) as a function of polymer to inorganic components mass ratio M. Fig. 5 indicates that the porosity of all films generally increased with increasing mass ratio M. However, some films synthesized using high mass ratio M showed reduced porosity. For example, the open porosity ϕ_o of the sol-gel mesoporous silica films prepared using Pluronic F127 increased from 22 to 65% as M increased from 0.4 to 2 g/g. However, ϕ_o decreased to 58% for M = 2.5 g/g. Similarly, the open and total porosities of the nanoparticle-based silica films, prepared using Pluronic P123, increased from 36 to over 63% when M increased from 0.2 to 1.5 g/g but ϕ_o decreased to 56% and ϕ to 60% for M = 2 g/g. This observation was likely due to the fact that
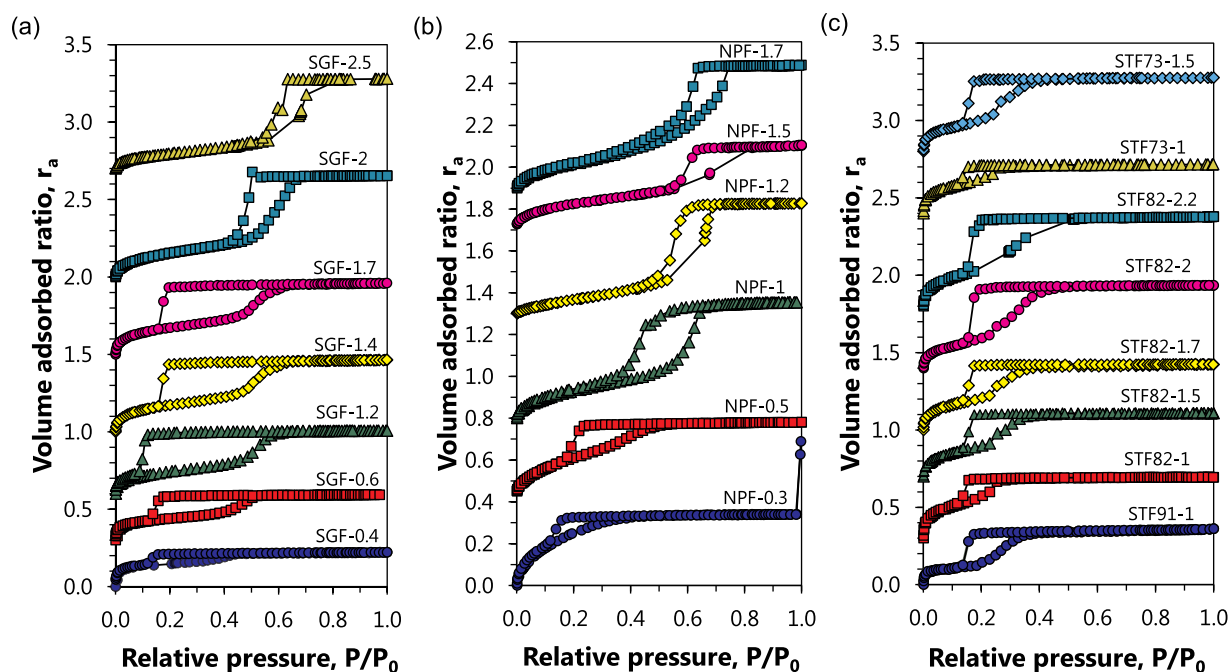

Fig. 4. Toluene adsorption-desorption isotherms measured by ellipsometric porosimetry of the (a) sol-gel mesoporous silica films, (b) nanoparticle-based mesoporous silica films, and (c) sol-gel mesoporous silica-titania films with silica:titania molar ratios of 90:10, 80:20, and 70:30 all prepared using Pluronic F127 with different polymer to inorganic components mass ratio M. Isotherms were shifted for better visibility.
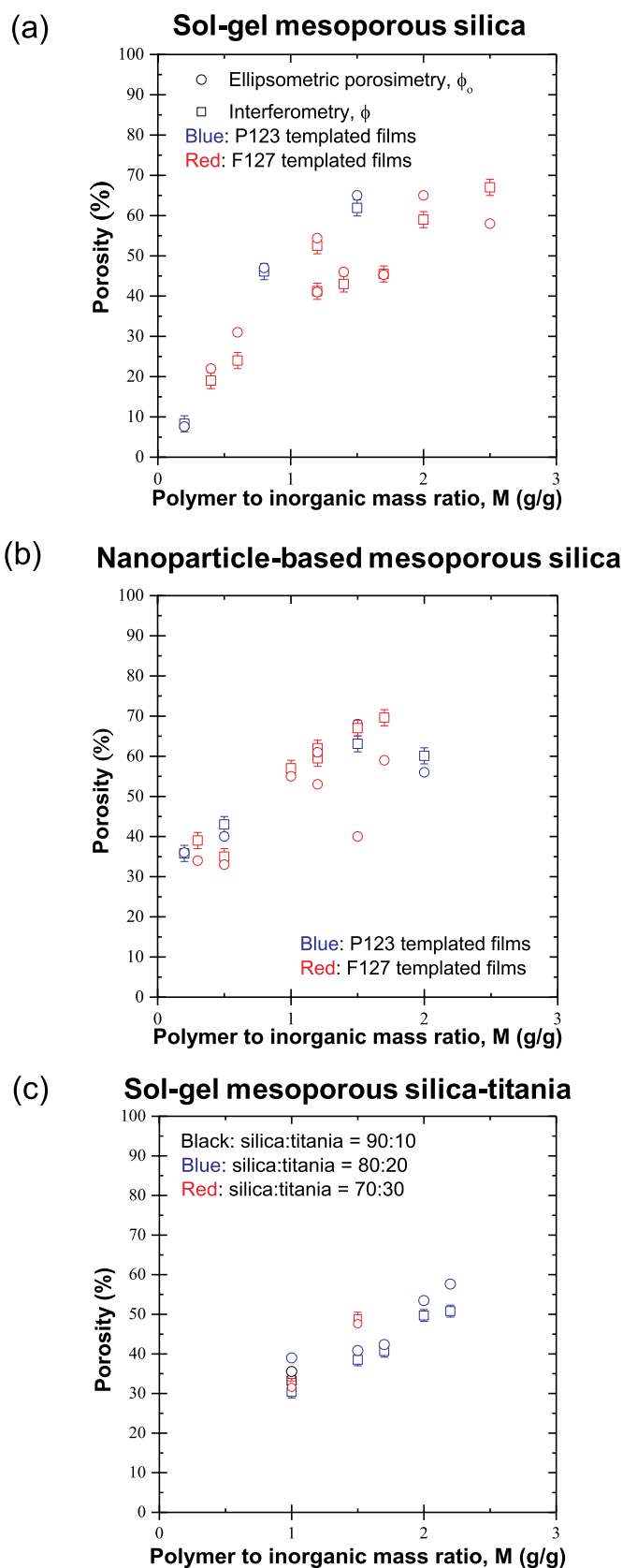
(a)

Sol-gel mesoporous silica

(b)

Nanoparticle-based mesoporous silica

(c)

Sol-gel mesoporous silica-titania

Fig. 5. Porosity as a function of the polymer to inorganic component mass ratio M for (a) sol-gel mesoporous silica, (b) nanoparticle-based mesoporous silica, and (c) sol-gel mesoporous silica-titania films measured by ellipsometric porosimetry and interferometry.

the films synthesized using high mass ratio M were more fragile, resulting in a partial collapse of the mesostructure during calcination. As a result, the porosity did not exceed 70% regardless of the polymer to inorganic components mass ratio M used for the synthesis.

Moreover, Fig. 5 shows that the minimum porosity of the sol-gel silica films was much lower (8% for $M = 0.2\,g/g$) than that of the nanoparticle-based silica films (34–36% for $M = 0.2$–$0.3\,g/g$). This can be attributed to the fact that condensation of molecular precursors formed a continuous silica network that, in the absence of polymer template, completely filled the available space forming dense silica films. By contrast, silica nanoparticles aggregate spontaneously and leave empty space between them, even for $M = 0\,g/g$, resulting in films with porosity above 26%, corresponding to the porosity of ordered close-packed monodisperse spheres [56].

4.2.4. Pore size distribution

Table 1 shows that the peak pore diameter d_p of the mesoporous silica and silica-titania films generally increased with increasing polymer to inorganic components mass ratio M. Moreover, Fig. 6 shows the pore size distributions retrieved from ellipsometric porosimetry for (a) sol-gel, (b) nanoparticle-based mesoporous silica, and (c) sol-gel mesoporous silica-titania thin films templated with Pluronic F127. They indicate that the pore size distributions of mesoporous silica films broadened with increasing mass ratio M. This was caused by the increase in block copolymer concentration that resulted in increasing micelles' size and broadening of their size distribution [53]. The latter also caused broadening of the neck size distribution reflected in the aforementioned changes of the hysteresis loops from H2(a) to H2(b) for the sol-gel mesoporous silica films (see Fig. 4(a) for SGF-0.4 to 2.5 and Fig. S4(a) for SGP-0.2 to 1.5). Finally, Fig. S5 shows similar trend for the pore size distributions of sol-gel and nanoparticle-based mesoporous silica films templated with Pluronic P123.

4.3. Comparison of characterization methods

Tables S3–S5 in Supporting Information summarize the thickness, spectral effective refractive index, and porosity measured by contact profilometry, interferometry, ellipsometric porosimetry, and/or nitrogen porosimetry of all synthesized films and their corresponding powders.

4.3.1. Film thickness L

Fig. 7(a) plots the thickness L of all mesoporous thin films investigated and measured using contact profilometry and interferometry as a function of the film thickness measured by ellipsometry. It shows that, in general, all three methods considered were consistent. In fact, the thickness measured by contact profilometry and interferometry fell within 10% of the value measured using ellipsometry. However, the thickness of the SGF-2.5, NPF-1.2-2, and NPP-1.5 films showed significant inconsistency among the three methods resulting in differences in excess of 10%. This was probably due to the non-uniformity of the film thickness since each method probed different parts of the film. Finally, note that the thickness of some mesoporous thin films less than ~ 250 nm thick and of dense silica-titania films could not be measured using contact profilometry because of the difficulty in preparing the samples due to the chipping of the films or the fact that they were too hard.

4.3.2. Effective refractive index $n_{eff,\lambda}$

Fig. 7(b) plots the effective refractive index $n_{eff,\lambda}$ measured at wavelength $\lambda = 500\,nm$ by interferometry as a function of that measured using ellipsometry for all mesoporous thin films investigated. It shows that the measurements from both methods fell within 5% of each other for all samples.
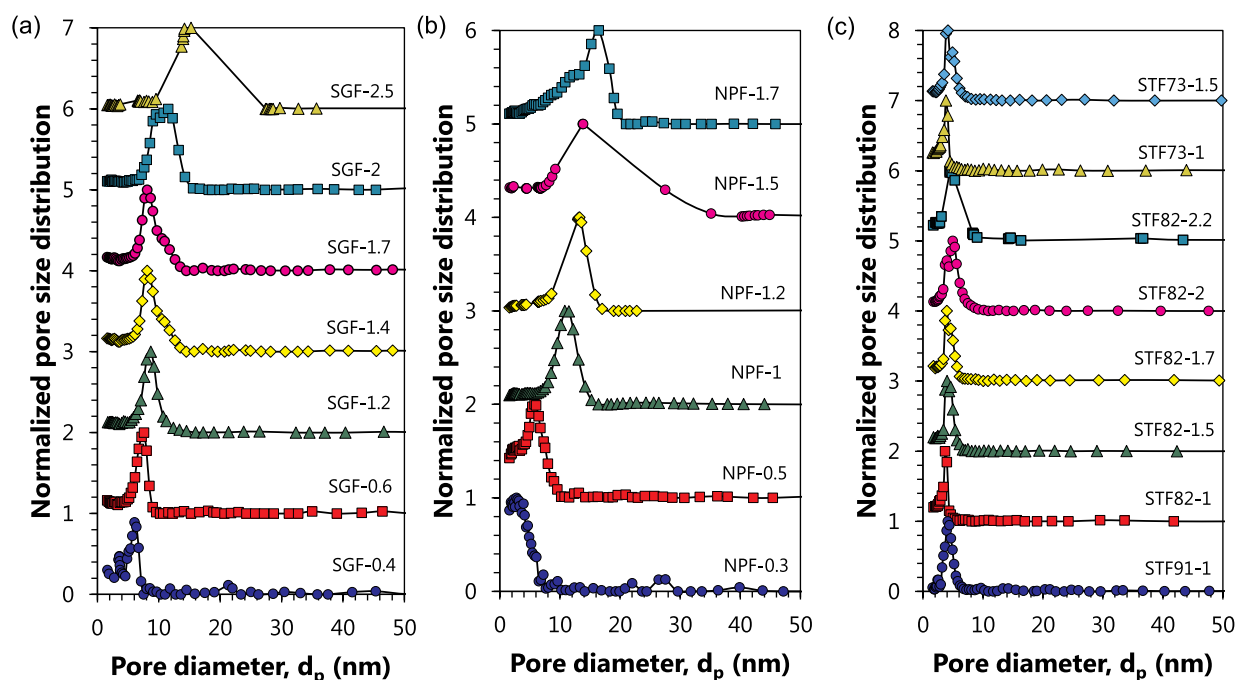
Fig. 6. Pore size distributions measured by ellipsometric porosimetry of the (a) sol-gel mesoporous silica films, (b) nanoparticle-based mesoporous silica films, and (c) sol-gel mesoporous silica-titania films with silica:titania molar ratios of 90:10, 80:20, and 70:30 all prepared using Pluronic F127 with different polymer to inorganic components mass ratio *M*. Pore size distributions were shifted by increments of 1.

4.3.3. Porosity

Fig. 7(c) plots the total porosity ϕ retrieved by interferometry using the Maxwell-Garnett EMA [Equation (2)] as a function of the open porosity ϕ_o measured by ellipsometric porosimetry, based on Lorentz-Lorenz EMA [Equation (11)], for all mesoporous thin films synthesized. It also shows the total porosity retrieved by ellipsometry using the measured effective refractive index and the Maxwell-Garnett EMA along with the open porosity measured from nitrogen adsorption porosimetry performed on equivalent powders. First, Fig. 7(c) shows that the total porosity ϕ measured by interferometry and ellipsometry agreed very well for most films. It also indicates that, for most samples, the total porosity obtained from interferometry was generally within 10% of the open porosity measured by ellipsometric porosimetry. This difference could be attributed to experimental uncertainty associated with both methods. It also suggests that the closed porosity of the films did not contribute significantly to their total porosity.

Fig. 7(c) also shows that the total porosity of several mesoporous films retrieved by interferometry or ellipsometry was unexpectedly lower than the open porosity measured with ellipsometric porosimetry. In the case of all mesoporous silica films and most mesoporous silica-titania films, the total and open porosities fell within a relative error of 15% or an absolute error of 7%. This may be due to experimental uncertainty associated with both methods. For sol-gel mesoporous silica-titania films, it may also be due to the fact that the sol-gel derived dense films used to retrieve $n_{c,\lambda}$ might have been slightly porous. This would lead to an underestimation of the refractive index $n_{c,\lambda}$ resulting in underestimation of the total porosity by interferometry based on the Maxwell-Garnett model. However, the differences observed were not significant and the accurate total and open porosities were within the experimental uncertainties.

Finally, the fact that the total porosity ϕ of most mesoporous silica-titania films measured by interferometry was in good agreement (within 10%) with that measured by ellipsometry establishes that interferometry is a simple and reliable method to estimate the porosity of multicomponent mesoporous films.

4.4. Mesoporous thin films versus equivalent powders

Tables S6 and S7 present the structural characteristics of the powders measured by nitrogen porosimetry. Powders were designated with the letter P followed by references to their structure (SG, NP, ST), the template used (F for Pluronic F127 or P for Pluronic P123), and the mass ratio *M*.

4.4.1. Structure

Fig. 8 shows the nitrogen adsorption-desorption isotherms of the powders equivalent to the (a) sol-gel mesoporous silica films, (b) nanoparticle-based mesoporous silica films, and (c) sol-gel mesoporous silica-titania films with silica:titania molar ratios of 90:10, 80:20, and 70:30, all prepared using Pluronic F127. Comparing Figs. 4 and 8 indicates that, in general, the equivalent powders had porous structures different from their corresponding thin films. For example, SGF-0.4 and SGF-0.6 films were mesoporous based on their type IV(a) toluene isotherms but their equivalent powders, P-SGF-0.4 and P-SGF-0.6, had isotherms of type I(a) according to the IUPAC classification indicating a microporous structure [1]. Moreover, for the SGF-1.7, SGF-2, SGF-2.5, NPF-1.2, NPF-1.5, and NPF-1.7 films, the toluene isotherms featured only one clear adsorption step related to the capillary condensation in the pores whereas the nitrogen isotherms of the corresponding powders featured two steps indicating a bimodal pore size distribution. These discrepancies can be attributed to the fact that sol-gel synthesis was very sensitive to the drying conditions [57] and that the drying rate in spin-coating of thin films was much larger than in synthesizing equivalent powders. The same observations were made for mesoporous silica films and powders templated with Pluronic P123 (Figs. S4 and S6).

4.4.2. Pore size distribution

Fig. 9 shows the pore size distributions measured by nitrogen porosimetry of the powders equivalent to the (a) sol-gel mesoporous silica films, (b) nanoparticle-based mesoporous silica films, and (c) sol-gel mesoporous silica-titania films with silica:titania molar ratio of 90:10, 80:20, and 70:30 all prepared with Pluronic F127. Comparing Figs. 6
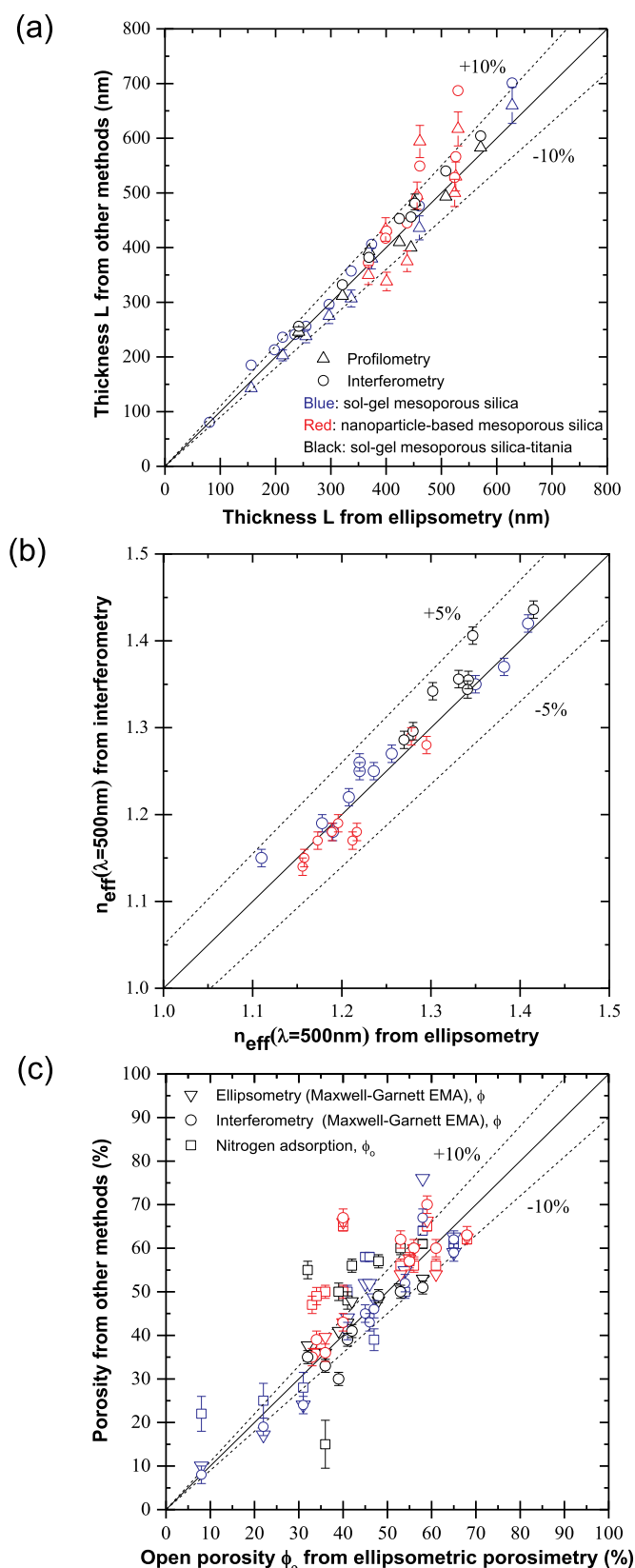
Fig. 7. (a) Thickness L, (b) effective refractive index $n_{eff}(\lambda = 500\,nm)$, and (c) porosity of sol-gel mesoporous silica films (Table S3), nanoparticle-based mesoporous silica films (Table S4), and sol-gel mesoporous silica-titania films (Table S5) measured by contact profilometry, interferometry, ellipsometry, and/or ellipsometric porosimetry. Dashed lines represent relative errors of 5 or 10%.

and 9 indicates that, overall, the pore size increased with increasing polymer to silica mass ratio *M* for both mesoporous thin films and powders. However, the films and their equivalent powders had different pore size distributions and peak pore diameter d_p. Contrary to the thin films, the powders often had bimodal pore size distributions such as P-SGF-1.4, P-SGF-1.7, or P-NPF-1.5 samples. Similar discrepancies could be observed for the sol-gel and nanoparticle-based mesoporous silica films and powders templated with Pluronic P123 (Figs. S5 and S7). This was due to the different drying conditions between the mesoporous films and the equivalent powders that affected their structural evolution, as previously discussed. Note that the kinetic diameter of toluene molecules is 0.61 nm [58] and that of nitrogen is 0.37 nm [59]. Therefore, since the measured pores featured a diameter equal or greater than 1.6 nm, both molecules should probe the same pore sizes [14].

4.4.3. Porosity

Fig. 7(c) indicates that the open porosity ϕ_o obtained from nitrogen porosimetry on the powders equivalent to the sol-gel mesoporous silica and silica-titania films generally differed by more than 10% from the open porosity ϕ_o of films measured by ellipsometric porosimetry. It is interesting to note that the porosity ϕ_o of the powders equivalent to the nanoparticle-based mesoporous silica films measured by nitrogen porosimetry was in good agreement (within 10%) with the porosity obtained from ellipsometric porosimetry or from interferometry in the case of the NPF-1.2, NPF-1.5, and NPF-1.7 films, except for films with low polymer to silica mass ratio $M \le 0.5\,g/g$.

Overall, these results establish that using the equivalent powders as a substitute to perform the structural characterization of thin films is inappropriate.

5. Conclusions

This study compared systematically contact profilometry, interferometry, ellipsometry, and ellipsometric porosimetry for measuring the thickness, effective refractive index, porosity, and/or pore size distribution of mesoporous thin films. To do so, mesoporous silica and silica-titania thin films with different thicknesses, structures (sol-gel or nanoparticle-based), compositions (silica or silica-titania), porosities, and pore sizes were synthesized and characterized. For most films, the thickness measured using contact profilometry and interferometry agreed within 15% with that measured using ellipsometry. Interferometry and ellipsometry should be preferred as they are non-destructive methods, unlike contact profilometry. The effective refractive index measured by interferometry agreed within 5% with that measured by ellipsometry. Finally, the porosity measured by interferometry fell within 15% with that measured by ellipsometric porosimetry for most films indicating that closed pores did not contribute significantly to the total porosity. Occasionally, interferometry was more appropriate for porosity measurements than ellipsometric porosimetry since it measures the total porosity of the film instead of the open porosity.

Moreover, the open porosity and pore size distribution measured by nitrogen adsorption porosimetry on equivalent powders disagreed with measurements made on the corresponding mesoporous thin films. These observations were attributed to the different drying conditions between spin coating of the films and drying of the powders. Therefore, characterization of equivalent powders cannot be used as representative of thin films. Overall, the study showed that interferometry is a robust and simple alternative to ellipsometry for measuring the film thickness, effective refractive index, and total porosity of non-absorbing multicomponent mesoporous thin films.

Supporting Information

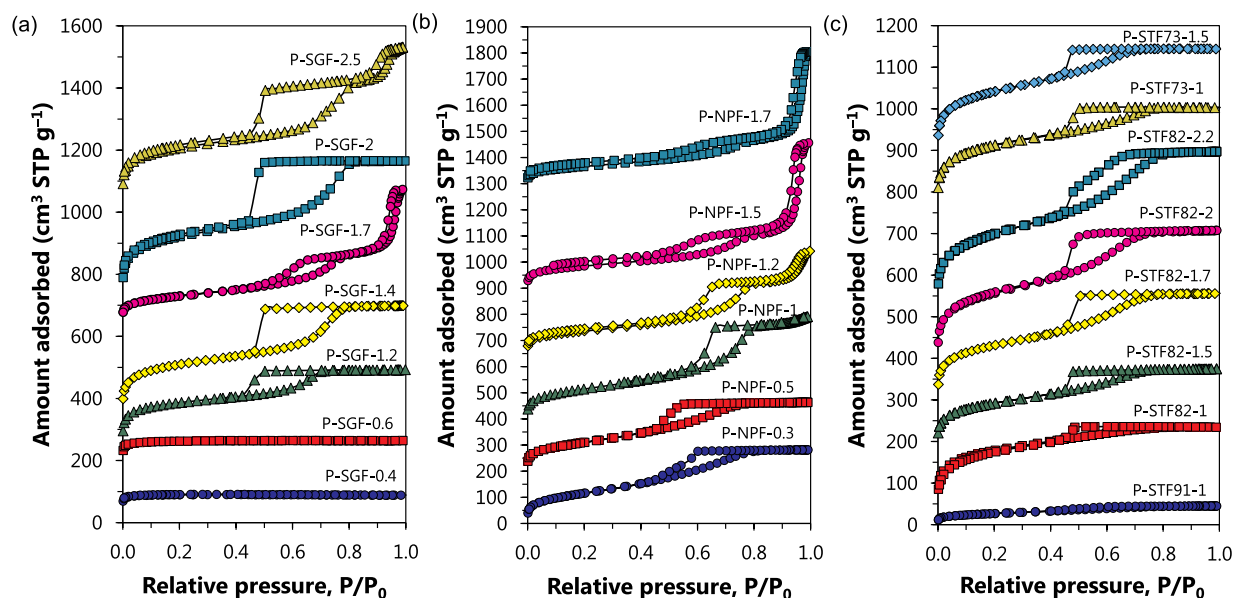Excel spreadsheets which can be used to retrieve the thickness,

Fig. 8. Nitrogen adsorption-desorption isotherms of the (a) sol-gel mesoporous silica powders, (b) nanoparticle-based mesoporous silica powders, and (c) sol-gel mesoporous silica-titania powders with silica:titania molar ratios of 90:10, 80:20, and 70:30 all prepared using Pluronic F127 with different polymer to inorganic components mass ratio *M*. Isotherms were shifted for better visibility.

effective refractive index, and porosity of mesoporous thin films from reflectance spectra using the interferometry method presented in this study. Full characterization procedures (section S1). Table for the coefficients *A*, *B*, and *C* [Equation (14)] for the index of refraction $n_{c,\lambda}$ of dense silica-titania films for different silica:titania molar ratios (Table S1). Table with thickness and effective refractive index of silica-titania dense films measured by ellipsometry and interferometry (Table S2). Tables with structural and optical characteristics of sol-gel and nanoparticle-based mesoporous silica thin films, sol-gel mesoporous silica-titania thin films, and their corresponding powders measured by contact profilometry, interferometry, ellipsometry, ellipsometric

porosimetry, and/or nitrogen adsorption porosimetry (Tables S3–S5). Tables with structural characteristics of sol-gel and nanoparticle-based mesoporous silica and sol-gel mesoporous silica-titania powders measured by nitrogen adsorption (Tables S6 and S7). Figure of the effective refractive index $n_{eff}(\lambda = 600$ nm) of mesoporous silica and silica-titania films as a function of their porosity ϕ (Fig. S1). Figures of block diagrams of (a) interferometry and (b) ellipsometric porosimetry (Fig. S2). Figure plotting the thickness and average refractive index of dense silica-titania films measured by interferometry as a function of those measured by ellipsometry (Fig. S3). Isotherms (Fig. S4) of sol-gel and nanoparticle-based mesoporous silica films templated with Pluronic
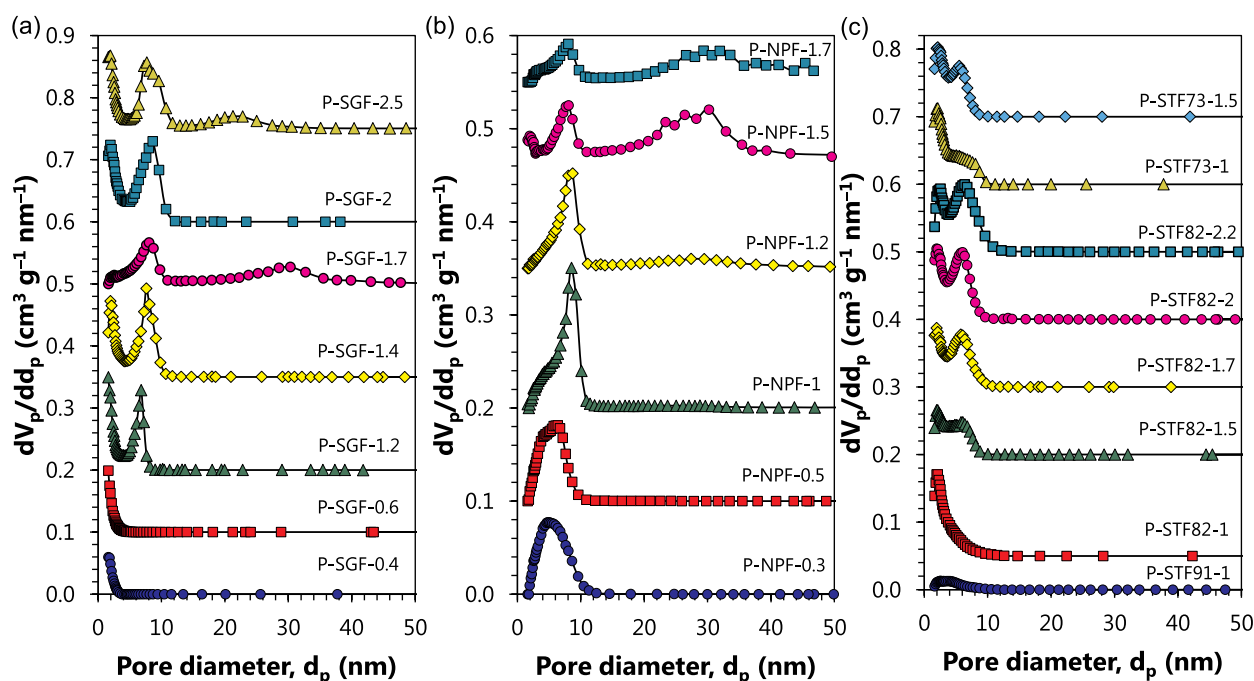

Fig. 9. Pore size distributions measured by nitrogen porosimetry of the (a) sol-gel mesoporous silica powders, (b) nanoparticle-based mesoporous silica powders, and (c) sol-gel mesoporous silica-titania powders with silica:titania molar ratios of 90:10, 80:20, and 70:30 all prepared using Pluronic F127 with different polymer to inorganic components mass ratio *M*. Pore size distributions were shifted for better visibility.

P123 and pore size distributions (Fig. S5). Isotherms of sol-gel and nanoparticle-based mesoporous silica powders templated with Pluronic P123 (Fig. S6). Pore size distributions of sol-gel and nanoparticle-based mesoporous silica powders templated with Pluronic P123 (Fig. S7).

Acknowledgment

Appendix A. Supplementary data

Supplementary data to this article can be found online at https://doi.org/10.1016/j.micromeso.2019.109677.

References

[1] M. Thommes, K. Kaneko, A. Neimark, J. Olivier, F. Rodriguez-Reinoso, J. Rouquerol, K. Sing, Pure Appl. Chem. 87 (9–10) (2015) 1051–1069 https://doi.org/10.1515/pac-2014-1117.
[2] O. Stenzel, The Physics of Thin Film Optical Spectra, Springer-Verlag, Heidelberg, Germany, 2005 https://doi.org/10.1007/978-3-319-21602-7.
[3] H.K. Raut, S.S. Dinachali, K.K. Ansah-Antwi, V.A. Ganesh, S. Ramakrishna, Nanotechnology 24 (50) (2013) 505201 https://doi.org/10.1088/0957-4484/24/50/505201.
[4] Z.-M. Qi, I. Honma, H. Zhou, J. Phys. Chem. B 110 (22) (2006) 10590–10594 https://doi.org/10.1021/jp061871j.
[5] H.-C. Kim, J.B. Wilds, C.R. Kreller, W. Volksen, P.J. Brock, V.Y. Lee, T. Magbitang, J.L. Hedrick, C.J. Hawker, R.D. Miller, Adv. Mater. 14 (22) (2002) 1637–1639 https://doi.org/10.1002/1521-4095(20021118)14:22<1637::AID-ADMA16373.0.CO;2-C.
[6] T. Coquil, E. Richman, N. Hutchinson, S. Tolbert, L. Pilon, J. Appl. Phys. 106 (3) (2009) 034910 https://doi.org/10.1063/1.3182826.
[7] A. Jain, S. Rogojevic, S. Ponoth, W. Gill, J. Plawsky, E. Simonyi, S.-T. Chen, P. Ho, J. Appl. Phys. 91 (5) (2002) 3275–3281 https://doi.org/10.1063/1.1448407.
[8] A. Jain, S. Rogojevic, S. Ponoth, N. Agarwal, I. Matthew, W. Gill, P. Persans, M. Tomozawa, J. Plawsky, E. Simonyi, Thin Solid Films 398 (2001) 513–522 https://doi.org/10.1016/S0040-6090(01)01311-6.
[9] B. Krause, G.-H. Koops, N.F. van der Vegt, M. Wessling, M. Wübbenhorst, J. van Turnhout, Adv. Mater. 14 (15) (2002) 1041–1046 https://doi.org/10.1002/1521-4095(20020805)14:15<1041::AID-ADMA10413.0.CO;2-A.
[10] R. Horvath, H.C. Pedersen, F.J. Cuisinier, Appl. Phys. Lett. 88 (11) (2006) 111102 https://doi.org/10.1063/1.2184756.
[11] M. Seino, W. Wang, J.E. Lofgreen, D.P. Puzzo, T. Manabe, G.A. Ozin, J. Am. Chem. Soc. 133 (45) (2011) 18082–18085 https://doi.org/10.1021/ja2080136.
[12] J.L. Hedrick, R.D. Miller, C.J. Hawker, K.R. Carter, W. Volksen, D.Y. Yoon, M. Trollsås, Adv. Mater. 10 (13) (1998) 1049–1053 https://doi.org/10.1002/(SICI)1521-4095(199809)10:13<1049::AID-ADMA1049>3.0.CO;2-F.
[13] M.Q. Brewster, Thermal Radiative Transfer and Properties, John Wiley & Sons, New York, NY, USA, 1992.
[14] J. Rouquerol, F. Rouquerol, P. Llewellyn, G. Maurin, K. Sing, Adsorption by Powders and Porous Solids: Principles, Methodology and Applications, Academic Press, Cambridge, MA, 2013 https://doi.org/10.1016/B978-0-12-598920-6.X5000-3.
[15] Y.K. Hwang, K.R. Patil, S.H. Jhung, J.-S. Chang, Y.J. Ko, S.-E. Park, Microporous Mesoporous Mater. 78 (2–3) (2005) 245–253 https://doi.org/10.1016/j.micromeso.2004.10.026.
[16] M. Baklanov, K. Mogilnikov, Microelectron. Eng. 64 (1) (2002) 335–349 https://doi.org/10.1016/S0167-9317(02)00807-9.
[17] M.T. Soo, G. Kawamura, H. Muto, A. Matsuda, Z. Lockman, K.Y. Cheong, Microporous Mesoporous Mater. 167 (2013) 198–206 https://doi.org/10.1016/j.micromeso.2012.09.010.
[18] Z. Li, S. Li, H. Luo, Y. Yan, Adv. Funct. Mater. 14 (10) (2004) 1019–1024 https://doi.org/10.1002/adfm.200305147.
[19] J. Kobler, T. Bein, ACS Nano 2 (11) (2008) 2324–2330 https://doi.org/10.1021/nn800505g.
[20] A. Sihvola, Electromagnetic Mixing Formulas and Applications vol. 47, The Institution of Electrical Engineers, London, UK, 1999.
[21] R. Gehr, R. Boyd, Chem. Mater. 8 (8) (1996) 1807–1819 https://doi.org/10.1021/cm9600788.
[22] M. Braun, L. Pilon, Thin Solid Films 496 (2) (2006) 505–514 https://doi.org/10.1016/j.tsf.2005.08.173.
[23] N. Hutchinson, T. Coquil, A. Navid, L. Pilon, Thin Solid Films 518 (8) (2010) 2141–2146 https://doi.org/10.1016/j.tsf.2009.08.048.
[24] M. Khardani, M. Bouaïcha, B. Bessaïs, Phys. Status Solidi C 4 (6) (2007) 1986–1990 https://doi.org/10.1002/pssc.200674420.
[25] E. Pedrueza, J. Valdés, V. Chirvony, R. Abargues, J. Hernández-Saz, M. Herrera, S. Molina, J. Martínez-Pastor, Adv. Funct. Mater. 21 (18) (2011) 3502–3507 https://doi.org/10.1002/adfm.201101020.
[26] D. Bouvard, J.-M. Chaix, R. Dendievel, A. Fazekas, J. Létang, G. Peix, D. Quenard, Cement Concr. Res. 37 (12) (2007) 1666–1673 https://doi.org/10.1016/j.cemconres.2007.08.028.
[27] M. Baklanov, K. Mogilnikov, V. Polovinkin, F. Dultsev, J. Vac. Sci. Technol. B 18 (3) (2000) 1385–1391 https://doi.org/10.1116/1.591390.
[28] P. Mezza, J. Phalippou, R. Sempere, J. Non-Cryst. Solids 243 (1) (1999) 75–79 https://doi.org/10.1016/S0022-3093(98)00825-4.
[29] D. Bruggeman, Ann. Phys. 416 (1935) 636–665.
[30] L. Lorenz, Ann. Phys. Chem. 247 (9) (1880) 70–103.
[31] H. Lorentz, Ann. Phys. Chem. 245 (4) (1880) 641–665.
[32] D. Aspnes, Thin Solid Films 89 (3) (1982) 249–262 https://doi.org/10.1016/0040-6090(82)90590-9.
[33] R. Cohen, G. Cody, M. Coutts, B. Abeles, Phys. Rev. B 8 (8) (1973) 3689–3703 https://doi.org/10.1103/PhysRevB.8.3689.
[34] M. Koledintseva, R. DuBroff, R. Schwartz, Prog. Electromagn. Res. 99 (2009) 131–148 https://doi.org/10.2528/PIER09091605.
[35] B. Schulz, High. Temp. - High. Press. 13 (6) (1981) 649–660.
[36] J. del Río, S. Whitaker, Transp. Porous Media 39 (2) (2000) 159–186 https://doi.org/10.1023/A:1006617029519.
[37] N. Hutchinson, T. Coquil, E. Richman, S. Tolbert, L. Pilon, Thin Solid Films 518 (8) (2010) 2134–2140 https://doi.org/10.1016/j.tsf.2009.08.006.
[38] D. Gonçalves, E.A. Irene, Quím. Nova 25 (5) (2002) 794–800 https://doi.org/10.1590/S0100-40422002000500015.
[39] E. Barrett, L. Joyner, P. Halenda, J. Am. Chem. Soc. 73 (1) (1951) 373–380 https://doi.org/10.1021/ja01145a126.
[40] L. Skinner, J. Sambles, J. Aerosol Sci. 3 (3) (1972) 199–210 https://doi.org/10.1016/0021-8502(72)90158-9.
[41] Semilab Co Ltd, Spectroscopic Ellipsometry Analyzer User's Reference Manual, (2012).
[42] S. Brunauer, P. Emmett, E. Teller, J. Am. Chem. Soc. 60 (2) (1938) 309–319 https://doi.org/10.1021/ja01269a023.
[43] M. Kruk, M. Jaroniec, Chem. Mater. 13 (10) (2001) 3169–3183 https://doi.org/10.1021/cm0101069.
[44] M. Jaroniec, M. Kruk, J. Olivier, Langmuir 15 (16) (1999) 5410–5413 https://doi.org/10.1021/la990136e.
[45] S.A. Chalmers, R.S. Geels, Thin-film metrology using spectral reflectance with an intermediate in-line reference, US Patent 7 (Mar. 10 2009) 502 119.
[46] V.A. Sterligov, Appl. Opt. 44 (21) (2005) 4538–4546 https://doi.org/10.1364/AO.44.004538.
[47] Y.K. Hwang, A.S. Mamman, K. Patil, L.K. Kim, J.S. Hwang, J.S. Chang, Solid State Phenomena, vol. 135, Trans Tech Publications, 2008, pp. 31–34 https://doi.org/10.4028/www.scientific.net/SSP.135.31.
[48] T. Matsubara, T. Oishi, A. Katagiri, J. Electrochem. Soc. 149 (2) (2002) C89–C93 https://doi.org/10.1149/1.1430718.
[49] C. Brinker, Y. Lu, A. Sellinger, H. Fan, et al., Adv. Mater. 11 (7) (1999) 579–585 https://doi.org/10.1002/(SICI)1521-4095(199905)11:7<579::AID-ADMA579>3.0.CO;2-R.
[50] C. Brinker, G. Scherer, Sol-Gel Science: the Physics and Chemistry of Sol-Gel Processing, Academic press, London, UK, 2013.
[51] D. Grosso, F. Cagnol, G.d.A. Soler-Illia, E. Crepaldi, H. Amenitsch, A. Brunet-Bruneau, A. Bourgeois, C. Sanchez, Adv. Funct. Mater. 14 (4) (2004) 309–322 https://doi.org/10.1002/adfm.200305036.
[52] D. Lee, D. Omolade, R.E. Cohen, M.F. Rubner, Chem. Mater. 19 (6) (2007) 1427–1433 https://doi.org/10.1021/cm070111y.
[53] D. Dunphy, P. Sheth, F.L. Garcia, C. Brinker, Chem. Mater. 27 (1) (2014) 75–84 https://doi.org/10.1021/cm5031624.
[54] I. Malitson, J. Opt. Soc. Am. 55 (10) (1965) 1205–1209 https://doi.org/10.1364/JOSA.55.001205.
[55] A. Forouhi, I. Bloomer, Phys. Rev. B 34 (10) (1986) 7018 https://doi.org/10.1103/PhysRevB.34.7018.
[56] F. Dullien, Porous Media: Fluid Transport and Pore Structure, Academic Press, London, UK, 2012.
[57] C. Brinker, G. Frye, A. Hurd, C. Ashley, Thin Solid Films 201 (1) (1991) 97–108 https://doi.org/10.1016/0040-6090(91)90158-T.
[58] S. Van der Perre, T. Van Assche, B. Bozbiyik, J. Lannoye, D.E. De Vos, G.V. Baron, J.F. Denayer, Adsorptive characterization of the zif-68 metal-organic framework: a complex structure with amphiphilic properties, Langmuir 30 (28) (2014) 8416–8424 https://doi.org/10.1021/la501594t.
[59] R.C. Weast, M.J. Astle, W.H. Beyer, et al., CRC Handbook of Chemistry and Physics vol. 69, CRC press, Boca Raton, FL, 1988.